

# CoFe/N, S-C Featured with Graphitic Nanoribbons and Multiple CoFe Nanoparticles as Highly Stable and Efficient Electrocatalysts for the Oxygen Reduction Reaction

Hongjie Meng, Supeng Pei, Hong Li,\* and Yongming Zhang\*



Cite This: *ACS Omega* 2021, 6, 11059–11067



Read Online

ACCESS |



Metrics & More

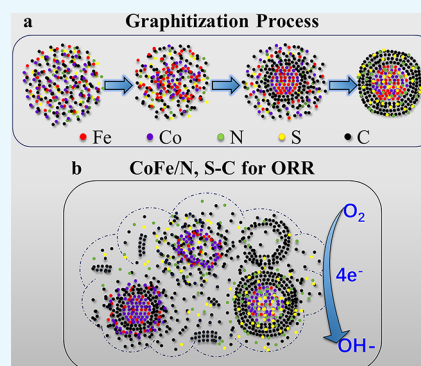


Article Recommendations



Supporting Information

**ABSTRACT:** The stability and activity of the catalysts are crucial for the oxygen reduction reaction (ORR) in fuel cells. Herein, CoFe/N, S-codoped biomass carbon (FB-CoFe-700) with graphitic nanoribbons and multiple CoFe nanoparticles was prepared through a facile thermal pyrolysis followed by an acid treatment process. The evolution of the growth of metal nanoparticles with the formation of graphite during the carbonization process was investigated. Inseparable from graphitic carbon-encased metal nanoparticles with the coexistence of graphitized nanoribbons and graphene-like sheets, FB-CoFe-700 exhibited a remarkable long-term electrocatalytic stability with 90.7% current retention after 50 000 s much superior to that of the commercially available Pt/C (20 wt %) in an alkaline medium. Meanwhile, FB-CoFe-700 displayed promising ORR catalytic activity ( $E_0 = 0.92$  V vs reversible hydrogen electrode (RHE),  $E_{1/2} = 0.82$  V vs RHE, and  $n = 3.97$ ) very similar to that of commercial Pt/C and outstanding methanol tolerance in an alkaline medium. This work is helpful for further development of nonprecious metal-doped carbon electrocatalysts with long-term stability.



## 1. INTRODUCTION

The electrochemical oxygen reduction reaction (ORR) at the cathode of polymer electrolyte fuel cells has attracted extensive attention due to the sluggish reaction kinetics.<sup>1–4</sup> Currently, platinum (Pt)-based electrocatalysts are considered to be the most effective catalysts for the ORR and have been widely used. Nevertheless, they still suffer from a series of problems, such as high price, scarce resources, long-term instability, CO poisoning, and poor methanol tolerance.<sup>5–8</sup> Moreover, the accumulation and dissolution of Pt nanoparticles from the carbon support due to carbon corrosion are key obstacles to an effective ORR.<sup>9–11</sup> Therefore, it is critical and desirable to develop alternative nonprecious metal catalysts with low cost and improved long-term stability.

Carbon-based materials have been regarded as one of the most promising candidates to replace the Pt-based catalysts for the ORR.<sup>12–14</sup> In particular, transition-metal-based carbonaceous materials doped with heteroatoms (such as N, P, S, B, and F) have attracted widespread attention due to their excellent electrocatalytic activity and high durability for the ORR.<sup>15–20</sup> The theoretical and experimental studies have proved that doping can introduce more defect sites in the six-membered carbon skeleton and redistribute the charge density and spin density, thereby enhancing the ORR performance of carbon materials.<sup>21</sup> Catalysts with graphitized carbon or graphitic layer-encapsulated metal particles usually possess excellent stability. The Co/CoO<sub>x</sub>@Co/N-graphene hybrid electrocatalyst, where the encapsulated Co/CoO<sub>x</sub> nano-

particles embed in Co/N-doped mesoporous graphene, demonstrated excellent ORR activity, outstanding long-term durability, and resistance to methanol poisoning.<sup>22</sup> Co-NC bamboolike carbon tubules (HP-Co-CNs) with core Co nanoparticles surrounded by ordered carbon layers showed superior ORR activities, excellent durability, and resistance to methanol in an alkaline medium.<sup>23</sup> Co-N-C nanofibers embedded with Co nanoparticles were prepared for oxygen reduction with high activity and remarkable durability.<sup>24</sup> Although these papers<sup>22–24</sup> have reported that transition metal nanoparticles encapsulated in ordered carbon layers/graphitic carbon/graphene can improve the stability of the catalyst, fewer reports investigated on the growth process and mechanism of transition metal-catalyzed graphitization during the pyrolysis and carbonization process.

Herein, we synthesized CoFe/N, S-codoped porous carbon with graphitic nanoribbons and multiple CoFe nanoparticles (denoted as FB-CoFe-700) using feculae bombycis (FB) and a metal source. FB intrinsically doped with N, S, and P was proved to be an excellent and environmentally friendly carbon source for ORR catalysts.<sup>25</sup> FB-CoFe-700 exhibits outstanding

Received: February 24, 2021

Accepted: April 1, 2021

Published: April 14, 2021



long-term stability, excellent methanol tolerance, and overall superior ORR catalytic activity compared to the commercial Pt/C in the alkaline medium, its catalytic activity is decreased for the ORR in acid medium. Moreover, iron and cobalt in the carbon matrix are found to promote the graphitization of amorphous carbon. The evolution of the growth of metal nanoparticles with the formation of graphite during the pyrolysis and carbonization process was investigated. The present result may offer in-depth information for the transition metal catalytic graphitization mechanism and is surely of great help to the design and preparation of future ORR catalysts with an excellent long-term stability.

## 2. EXPERIMENTAL SECTION

**2.1. Materials and Chemicals.** FB was produced by silkworms raised by ourselves. Methanol ( $\text{CH}_3\text{OH}$ ), ethanol ( $\text{CH}_3\text{CH}_2\text{OH}$ ), potassium hydroxide (KOH),  $\text{H}_2\text{SO}_4$  (98%), ferric nitrate nonahydrate ( $\text{Fe}(\text{NO}_3)_3 \cdot 9\text{H}_2\text{O}$ ), cobalt nitrate hexahydrate ( $\text{Co}(\text{NO}_3)_2 \cdot 6\text{H}_2\text{O}$ ), commercial Pt/C (20 wt %, JM), and 5 wt % Nafion solution were used as received.

**2.2. Preparation of FB-CoFe-600, FB-CoFe-700, and FB-CoFe-800.** Briefly, 0.8 g  $\text{Fe}(\text{NO}_3)_3 \cdot 9\text{H}_2\text{O}$  and 0.5 g  $\text{Co}(\text{NO}_3)_2 \cdot 6\text{H}_2\text{O}$  were dissolved in 50 mL deionized water, and then 2.5 g FB was soaked in the obtained nitrate solution with magnetic stirring for 12 h and vacuum drying at 80 °C overnight to obtain a solid mixture. The obtained mixture subsequently was transferred to a porcelain boat and carbonized in the center of the tube furnace at 600, 700, and 800 °C (Ar atmosphere, 2 h with a heating rate of 5 °C  $\text{min}^{-1}$ ). After the pyrolysis process of the mixture, the products were etched with 0.5 M  $\text{H}_2\text{SO}_4$  solution for 12 h and then washed with deionized water until the pH of the residual water was neutral and finally dried at 80 °C for 8 h in a vacuum oven. The as-prepared samples calcined at 600, 700, and 800 °C were denoted as FB-CoFe-600, FB-CoFe-700, and FB-CoFe-800, respectively. FB-Co-700 (without acid treatment) was prepared with an equal mass of  $\text{Co}(\text{NO}_3)_2 \cdot 6\text{H}_2\text{O}$  instead of the mixture of  $\text{Co}(\text{NO}_3)_2 \cdot 6\text{H}_2\text{O}$  and  $\text{Fe}(\text{NO}_3)_3 \cdot 9\text{H}_2\text{O}$  compared with FB-CoFe-700.

## 3. RESULTS AND DISCUSSION

**3.1. Formation and Morphology of the Catalysts.** FB-CoFe-600, FB-CoFe-700, and FB-CoFe-800 were prepared by the pyrolysis of FB with  $\text{Fe}(\text{NO}_3)_3 \cdot 9\text{H}_2\text{O}$  and  $\text{Co}(\text{NO}_3)_2 \cdot 6\text{H}_2\text{O}$  at temperatures of 600, 700, and 800 °C, respectively, followed by an acid etching process. The acid treatment can remove some aggregates of metal and impurities, thereby increasing the active specific surface area. The morphology and structure of FB-CoFe-600, FB-CoFe-700, and FB-CoFe-800 are characterized by scanning electron microscopy (SEM) (Figure 1). It can be seen that compared to FB-CoFe-600 with a compact thick layer structure as shown in Figure 1a, FB-CoFe-700 and FB-CoFe-800 shown in Figure 1b,c exhibit a

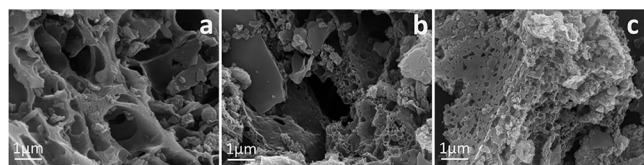


**Figure 1.** SEM images of (a) FB-CoFe-600, (b) FB-CoFe-700, and (c) FB-CoFe-800.

significantly more extended structure and abundant pores, indicating that the increased temperature is conducive to the expansion of the pore structure. In addition, the corresponding elemental mapping images of the three samples shown in Figure S1 directly signify the presence and homogeneous distribution of nitrogen, sulfur, and cobalt (N, S, and Co) in the carbon matrix. The well-constructed pore structure and uniformly distributed elements can facilitate the transport of  $\text{O}_2$  and expose more active sites during the ORR catalytic process. The element contents of Fe and P were indeed too low to be detected by energy dispersive spectroscopy (EDS) due to the escape of the P element in the pyrolysis process and the removal of Fe or  $\text{Fe}_x\text{Y}$  (Y = N, P, S, and O) by acid etching, but they can be measured by inductively coupled plasma (ICP). The resulting elemental compositions of FB-CoFe-600, FB-CoFe-700, and FB-CoFe-800 are shown in Table 1.

**Table 1.** Elemental Composition of FB-CoFe-600, FB-CoFe-700, and FB-CoFe-800 Tested by ICP

sample	C (%)	S (%)	P (%)	Co (%)	Fe (%)
FB-CoFe-600	96.30	1.24	0.04	1.89	0.53
FB-CoFe-700	96.27	1.20	0.04	1.98	0.51
FB-CoFe-800	93.33	2.88	0.36	2.22	1.21

To obtain further detailed structural information, transmission electron microscopy (TEM) characterization of FB-CoFe-700 is performed, and the images are shown in Figure 2.

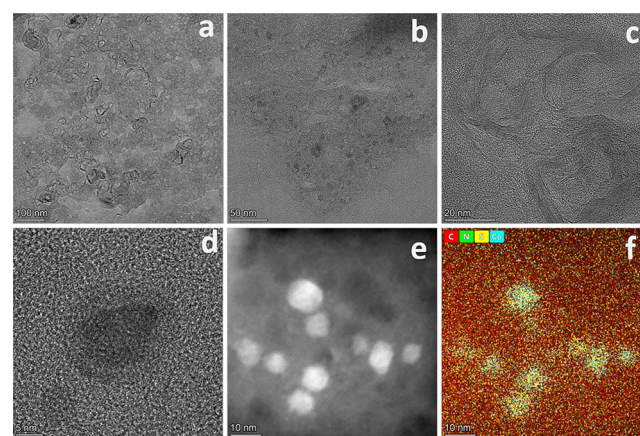


**Figure 2.** TEM (a and b), HRTEM (c and d), and HAADF and the corresponding elemental mapping images of FB-CoFe-700 (e and f).

The coexistence of graphitized nanoribbons, graphene-like sheets, and small-sized metal particles in the carbon matrix can be observed in Figure 2a. Figure 2b shows that the cobalt nanoparticles with sizes of 5–10 nm are uniformly dispersed in the porous carbon. Figure 2c displays the more clearly enlarged image of graphitized nanoribbons and graphene-like sheets. Moreover, the outline of the encapsulation circle around the metal nanoparticles is obvious in Figure 2d, although the lattice fringes of the encapsulating substance cannot be seen clearly. It is presumable that the graphitization in the carbon matrix and the encapsulation around the metal particles should be conducive to the stability of the catalyst. The HAADF and elemental mapping images of FB-CoFe-700 are shown in Figures 2e,f and S2, where C and N elements are evenly distributed, P element is almost invisible due to its extremely

low content, and the S element highly overlaps with the metal nanoparticles, and this may attributed to the inevitable residue of sulfates, although the final wash solution of the samples after the pickling process is colorless and neutral. In addition, there is another possibility that the S element in FB is inherently inclined to combine with Co.<sup>26</sup> Follow-up exploration will continue for this issue.

How did the above-mentioned graphitized nanoribbons/graphene-like sheets/graphitized layer around the metal particle form? Because the empty d-orbital of group VIII metals (such as Fe, Co, and Ni) can accept electrons from carbon (carbon in metals is a positive ion),<sup>27</sup> transition metals could melt the carbon easily and form a solid solution of transition metals and carbon. When the carbon in the solid solution reached saturation, the saturated carbon tended to form more stable graphitic carbon with low energy and deposited on the surface of the metal particles. The metal aggregated and grew toward the nucleus, while the saturated carbon was precipitated to form graphite or easily graphitized carbon, and the easily graphitized carbon can be further converted into graphite.<sup>28</sup> It has been reported that at a certain temperature (usually 600 °C and above), the scattered Ni fragments could quickly move on the amorphous carbon (a-C) and leave a graphitized trace behind. When the Ni particle was directly placed on the a-C substrate, Ni could graphitize the surrounding a-C and make the Ni particle itself encapsulated by the graphite layers. A typical catalytic process of Fe particles with the a-C support film revealed that the gradually increased temperature resulted in some active Fe particles spreading on the a-C substrate to coalescence to larger particles by the incorporation of neighboring particles and left their “footprints,” remnants of graphite nanoribbons/shells.<sup>29</sup> The higher the temperature, the faster the spreading of the metal particles, and the higher the activity of the metal for catalyzing graphitization. Herein, the metal ions dispersed in the precursor matrix gradually broke away from the bondage to aggregate, with an increase in the temperature, and then formed into irregular rings or small metal core centers, preliminarily graphitizing the a-C in their propagation pathway (graphitized nanosheets/ribbons before acid treatment). Moreover, in the phase where metal and carbon coexist, metal atoms always tend to be closely packed, thereby minimizing the surface energy to reach a steady state. Driven by this power,<sup>30</sup> the metal atoms gradually grow toward the solid particles and promote the migration of surrounding carbon atoms to the surface to form a graphitized/ordered carbon layer. As the metal particles grow and the temperature rises, the graphitization is gradually improved and the structure becomes clear gradually. Finally, when the metal particle is completely coated with graphitized carbon layers, the growth of the carbon layer stops; the schematic illustration of the metal-catalyzed graphitization is depicted in Scheme 1.

In addition, Figure 2b shows that some metal nanoparticles appear like core–shell structures accompanied by partly hollow structures. It is uncertain whether these hollow/core–shell capsule structures are the result of the incomplete acid etching. Therefore, TEM tests for the samples before acid etching were implemented. As shown in Figure 3a–f for FB-CoFe-700 before acid etching, cobalt nanoparticles with hollow, core–shell, or solid structures uniformly dispersed in the carbon matrix, which indicates that these structures have been formed during pyrolysis. However, how were these structures formed? Based on the above explanation for metal-catalyzed graphitiza-

### Scheme 1. Schematic Illustration of Metal-Catalyzed Graphitization

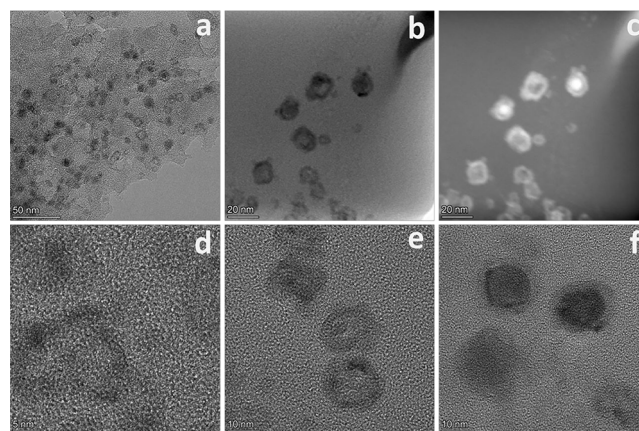
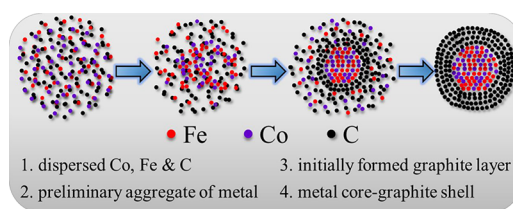


**Figure 3.** (a and b) TEM, (c) HAADF, and (d–f) HRTEM of FB-CoFe-700 before acid etching.

tion, we infer that the scattered metal ions in the carbon matrix first tend to aggregate, and the random-directional aggregation, spreading, and fusion process of metals form hollow structures or initially fused solid particles (Figure 3c–e).<sup>31</sup> Second, with further aggregation of metals, the metals gradually stack toward the metal core in a more orderly and compact manner (crystallize), while the outer boundary of the particles can merge with other neighboring small particles and fuse their metal and carbon, thereby forming a core–shell structure with the metal in both the core and the shell. Then, the particle size gradually increases until the metal nucleus is completely encapsulated by the graphite carbon layers to form a complete metal core–graphite shell structure (Figure 3c,f).<sup>30,32</sup> Therefore, a state where metals distribute in both the core and the shell of different structures in FB-CoFe-700 can be seen in Figure 3c.

To further study and verify the effect of temperature on the formation process of metal-catalyzed graphitization, TEM characterizations of FB-CoFe-600, FB-CoFe-700, and FB-CoFe-800 before acid etching were further performed. As can be seen from Figure 4, the dispersed metal in the carbon matrix showed the rudiment of the particles but with fuzzy boundary at 600 °C (Figure 4a,d). The particles further grew more distinctly at 700 °C and possessed different structures that can be clearly distinguished, including hollow structures, core–shell structures, and solid nanoparticles (Figure 4b,e). When the temperature rose to 800 °C, the particles were significantly larger and coexisted with core–shell structure and solid particles, while almost no hollow structures were visible (Figure 4c,f). As the temperature increased, the contour of the metal particles gradually became clear from the blur boundary during the growth process of metal particles, which may also be confirmed in the element distribution mapping shown in Figure S3. The gradually clear particle contour profile with the

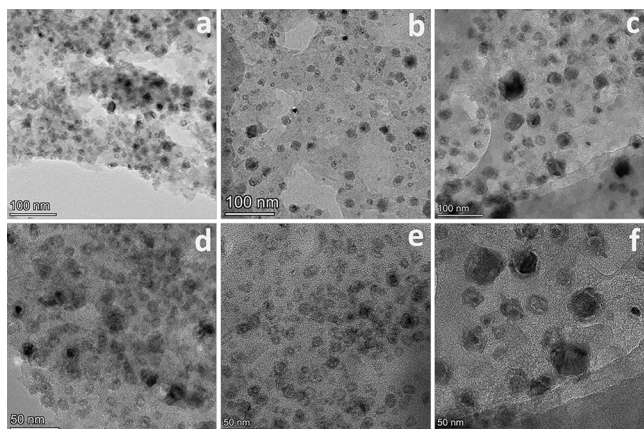


**Figure 4.** TEM comparison of (a and d) FB-CoFe-600, (b and e) FB-CoFe-700, and (c and f) FB-CoFe-800 before acid etching.

increasing temperature indicates that gathering and growth of the metals propagating toward the metal nucleus are more compact. However, the process of more compact aggregation of metals toward the core is also the process in which the eutectic carbon in solid solution is pushed outward to form graphitized carbon at the metal–graphite interface. Therefore, the clearer the particle boundary, the tighter the stacking of the metal in the particles, and the more perfect the graphite encapsulation.<sup>31</sup> In addition, the nanoscale porous structure in FB-CoFe-700 may originate from the capsular graphitized patterns left by the removed metal particles during acid washing (Figure S4a,b). However, the graphitized nanoribbons and graphene-like sheets in the carbon matrix of FB-CoFe-700 before acid etching should be attributed to the graphitized trace left by the initial aggregation and migration of active metals on the a-C substrate (Figure S4c,d).<sup>29–31</sup>

**3.2. Structure and Composition of FB-CoFe-600, FB-CoFe-700, and FB-CoFe-800.** In addition to the morphological structure, further detailed physical properties were characterized. The BET specific surface areas (SSAs) and pore-size distributions of the three samples were investigated through N<sub>2</sub> adsorption curves. According to the IUPAC classification, FB-CoFe-600, FB-CoFe-700, and FB-CoFe-800 in Figure 5a show type-IV isotherms with SSAs of 368.2, 311.5, and 318.1 m<sup>2</sup> g<sup>-1</sup>, respectively, which indicate that they possess mesoporous structures.<sup>33</sup> Moreover, compared with FB-CoFe-600 (5.4 nm), FB-CoFe-700 and FB-CoFe-800 possess slightly lower SSAs but significantly increased average pore sizes of 6.3 and 10.2 nm, respectively (Figure 5b), especially the generation of the macroporous structure for FB-CoFe-800,

which corresponds to the steep rise at the higher relative pressure belonging to the type-II isotherm shown in Figure 5a.<sup>34</sup> This is because as the temperature increases, the decomposition of the nitrate and organic matter in FB was more thorough, and further extension of the pore structure results in the shift of small holes to larger holes and partial breakage of the larger pores; hence, the BET is slightly reduced but the average pore sizes were increased substantially. In addition, when it reached 800 °C, the excessive destruction of the pore structure led to the reduced pore volume. However, the well-constructed mesoporous structure and higher pore volume can facilitate the mass transfer, thereby being conducive to the ORR. Thus, FB-CoFe-700 may be the superior choice.

The XRD profiles in Figure S5a show that all of the FB-CoFe-600, FB-CoFe-700, and FB-CoFe-800 have two broad peaks located at around 25.0° and 42.8° that were assigned to the characteristic carbon (002) and (100) diffractions, while a minor sharp profile at 26.6° can be observed, suggesting that the graphitized material underwent metal-catalyzed graphitization during the carbonization.<sup>27</sup> In addition, as the temperature increases, the obvious positive shift of the (100) peak for the three samples suggests that the interplanar spacing and graphitization degree decrease due to the lattice distortion, defects, and amorphization caused by macroscopic stress due to the elevated temperatures.

The Raman spectra in Figure S5b show three main peaks at around 1338, 1594, and 2830 cm<sup>-1</sup> corresponding to the D-band (defective sp<sup>3</sup> carbon), G-band (graphitic sp<sup>2</sup> carbon), and 2D-band. The 2D band is a prominent feature of a higher graphitic degree. The intensity ratio (*I*<sub>D</sub>/*I*<sub>G</sub>) reflects the defect level of the graphitic structure.<sup>35</sup> The integrated *I*<sub>D</sub>/*I*<sub>G</sub> values of FB-CoFe-600, FB-CoFe-700, and FB-CoFe-800 are 2.4, 2.6, and 2.9, respectively, which indicates that the higher the temperature, the lower the graphitization. This is because the higher the temperature, the more the extension and exposure of the carbon material structure, and the more the defects generated after pickling. Furthermore, the intensity change in the 2D peak of the three samples is a strong evidence of the above results.<sup>36</sup>

The XPS survey spectra together with the high-resolution N 1s, S 2p, and Co 2p spectra of FB-CoFe-600, FB-CoFe-700, and FB-CoFe-800 were further characterized to study their chemical nature, as shown in Figures 6 and S6. The N species can be deconvoluted into five contributions in the high-resolution N 1s, which are attributed to the oxidized-N (402.8 eV), graphitic-N (401.1 eV), pyrrolic-N (400.3 eV), pyridinic-N (398.2 eV), and Co-N (399.2 eV).<sup>37,38</sup> In the S 2p XPS

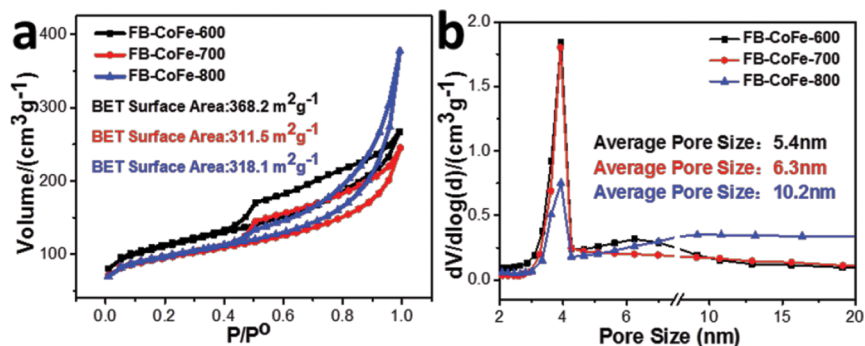


**Figure 5.** (a) N<sub>2</sub> adsorption/desorption isotherms and (b) pore size distributions of FB-CoFe-600, FB-CoFe-700, and FB-CoFe-800.

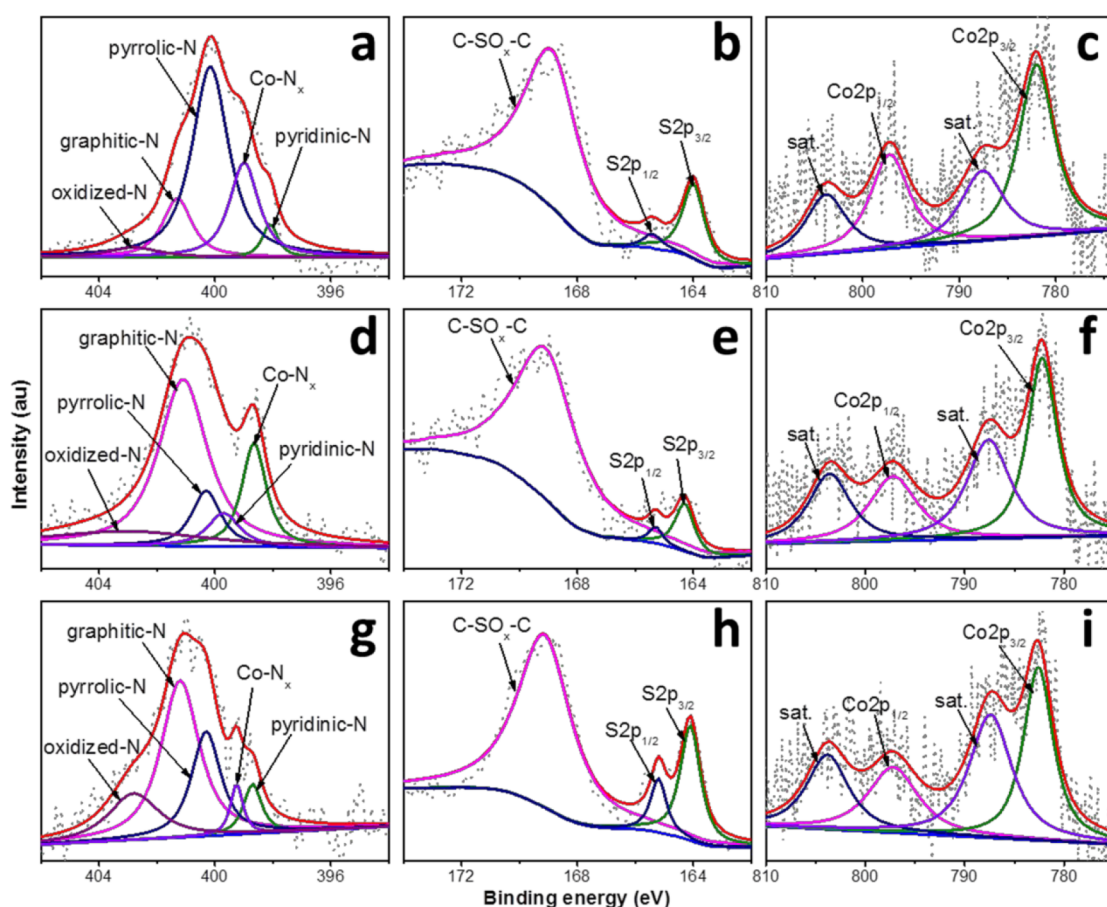


**Figure 6.** High-resolution XPS spectra of N 1s, S 2p, and Co 2p for (a–c) FB-CoFe-600, (d–f) FB-CoFe-700, and (g–i) FB-CoFe-800.

spectrum, two strong peaks at 164.3 and 165.4 eV are assigned to S 2p<sub>3/2</sub> and S 2p<sub>1/2</sub> of the Co–S bond, respectively,<sup>39</sup> indicating the presence of Co–S bonds in the prepared samples. Compared with the standard peaks at 161.5 and 162.5 eV, the positive shift of the peak position indicates strong bonding between Co and S.<sup>40</sup> Meanwhile, the peak at 169.2 eV is assigned to C–SO<sub>x</sub>–C species.<sup>41</sup> The Co 2p spectrum shows Co 2p<sub>3/2</sub> and Co 2p<sub>1/2</sub> peaks at 782.2 and 797.2 eV (standard peaks at about 780.9 and 795.3 eV)<sup>32,42</sup> with two satellite peaks (787.6 and 803.6 eV),<sup>39,41,43</sup> which also reveals that the Co–S/Co–N bonds might exist in the composite. The certain shift of Co 2p bonding energies suggests a strong interaction between the carbon material and Co NPs.<sup>44</sup> Combining the overlapped elemental mapping images of S and Co in Figure S2 and these XPS analyses, it can be deduced that the surface of Co NPs has a strong bonding force with sulfur elements in the prepared samples.

As can be seen from the elemental content of the samples tested by ICP and XPS in Tables 1 and 2, with an increase in the temperature, the C content increases and the contents of heterogeneous elements such as O and N gradually decreased, which is a common trend, while the content of S gradually increased uncharacteristically. At the same time, the content of Co also gradually increased. Comprehending the mapping images of S and Co in Figure S2 and the above analysis of Co 2p and S 2p spectra, the abnormally increased contents of Co and S may be attributed to the residual cobalt sulfate during the sulfuric acid pickling process. Besides, as the temperature increases, pyrrole-N, which is not effective for ORR, gradually transforms into graphite-N and pyridinic-N, which are active

**Table 2. Elemental Composition of FB-CoFe-600, FB-CoFe-700, and FB-CoFe-800 by XPS**

sample	C 1s (%)	O 1s (%)	N 1s (%)	S 2p (%)	Co 2p (%)
FB-CoFe-600	77.42	17.39	2.89	0.92	1.38
FB-CoFe-700	78.94	15.57	2.32	1.28	1.88
FB-CoFe-800	80.0	15.0	1.12	2.03	2.1
sample	graph-N (%)	pyrid-N (%)	pyro-N (%)	Co-N <sub>x</sub> (%)	oxid-N (%)
FB-CoFe-600	13.8	4.2	54.86	22.16	4.98
FB-CoFe-700	52.08	16.2	10.37	6.83	14.52
FB-CoFe-800	46.43	7.0	23.6	4.93	23.6
sample	C-SO <sub>x</sub> -C (%)	S 2p <sub>3/2</sub> (%)	S 2p <sub>1/2</sub> (%)	Co 2p <sub>1/2</sub> (%)	Co 2p <sub>3/2</sub> (%)
FB-CoFe-600	81.7	15.7	2.6	24.1	40.6
FB-CoFe-700	86.3	9.9	3.8	19.7	34.5
FB-CoFe-800	74.5	18.7	6.8	19.6	30.8

sites for the ORR, and achieve the best synergy with other efficient Co–N<sub>x</sub>/Co–S<sub>x</sub> active sites at 700 °C.

The Co content tested by XPS at 600 °C is slightly lower than that by ICP, which should be attributed to the fact that the structure of FB-CoFe-600 is not fully stretched at a relatively lower temperature, and some cobalt particles are buried inside the carbon matrix. However, the content of Co tested by XPS at 700 and 800 °C is close to that by ICP, which may be attributed to the part of residual cobalt sulfate on the porous carbon surface of FB-CoFe-700 and FB-CoFe-800 together with the more exposed cobalt nanoparticles in the much more extended porous structure. In addition, the P and

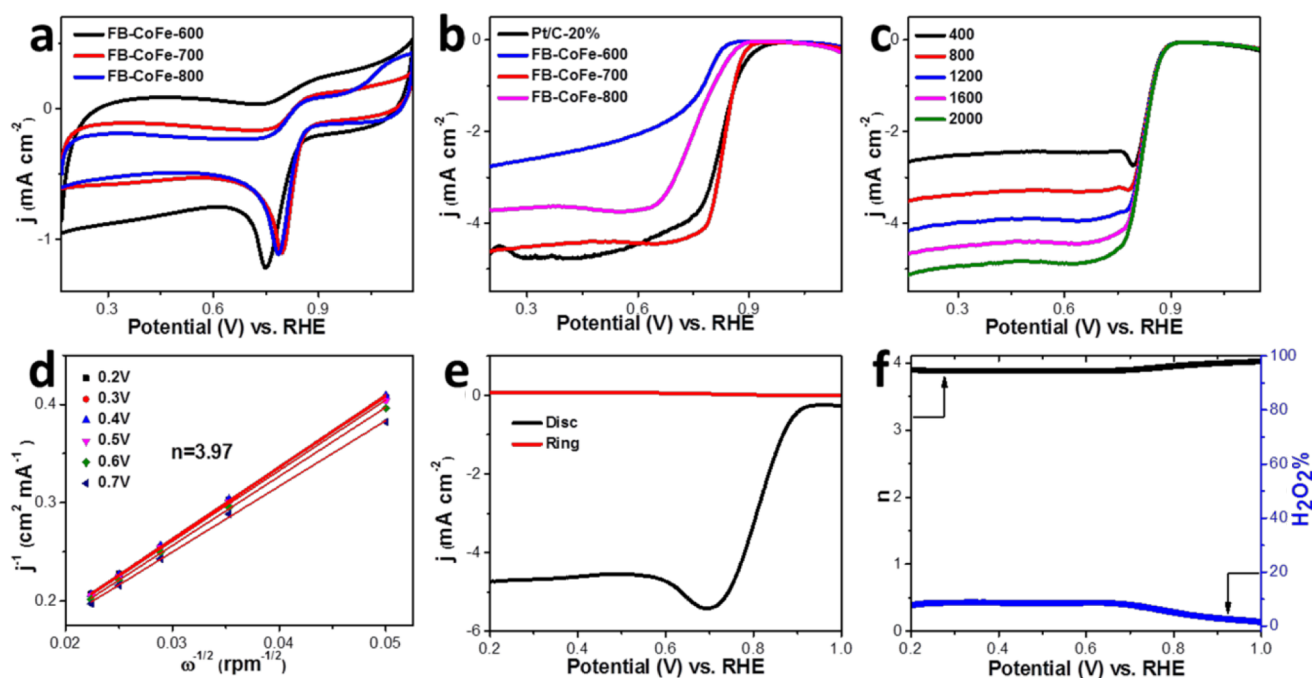


**Figure 7.** (a) CV curves of FB-CoFe-600, FB-CoFe-700, and FB-CoFe-800. (b) LSV curves of FB-CoFe-600, FB-CoFe-700, FB-CoFe-800, and Pt/C 20% at a rotation speed of 1600 rpm. (c) LSV curves and (d) K–L plots of FB-CoFe-700. (e) RRDE curves of FB-CoFe-700 at a rotation speed of 1600 rpm. (f)  $\text{H}_2\text{O}_2$  and electron transfer number of FB-CoFe-700 at 1600 rpm. All the tests were carried out in  $\text{O}_2$ -saturated 0.1 M KOH with a scan rate of  $10 \text{ mV s}^{-1}$ .

Fe elements cannot be detected by XPS for the prepared samples due to the extremely low content of P and the acid etching of Fe from the sample surface, which is consistent with the ICP results. As for the Fe element, it can be seen that Fe and Co coexist in an overlapping state in metal particles in the elemental distribution mapping of FB-CoFe-700 without acid etching (Figure 3). Although most Fe was etched away preferentially in the acid treatment process for FB-CoFe-700 due to the higher metal activity than Co, this may result in a larger exposed active surface of Co. We speculate that Fe acted like a sacrificed template, turning crystalline CoFe alloy particles into sievelike Co particles rich in defects and vacancies, thereby increasing their specific surface activity.

**3.3. Electrocatalytic Activities toward the ORR of FB-CoFe-600, FB-CoFe-700, and FB-CoFe-800.** The ORR electrocatalytic activities of FB-CoFe-600, FB-CoFe-700, and FB-CoFe-800 were first evaluated by CV (Figure 7a). In comparison with FB-CoFe-600 and FB-CoFe-800, FB-CoFe-700 exhibits an obvious more positive oxygen reduction peak centered at 0.80 V versus RHE. To gain further insight into their electrocatalytic activity, LSV curves were recorded via a rotating disc electrode (RDE) in the  $\text{O}_2$ -saturated 0.1 M KOH electrolyte. As shown in Figure 7b, compared with FB-CoFe-600 ( $E_0 = 0.86 \text{ V vs RHE}$ ) and FB-CoFe-800 ( $E_0 = 0.90 \text{ V vs RHE}$ ;  $E_{1/2} = 0.76 \text{ V vs RHE}$ ), FB-CoFe-700 presented a much more positive onset potential ( $E_0 = 0.92 \text{ V vs RHE}$ ) and a better half-wave potential ( $E_{1/2} = 0.82 \text{ V vs RHE}$ ) that are extremely close to those of the commercial Pt/C ( $E_0 = 0.94 \text{ V vs RHE}$ ;  $E_{1/2} = 0.82 \text{ V vs RHE}$ ), which indicates that FB-CoFe-700 possesses the most excellent ORR electrocatalytic properties. On the one hand, the cobalt species that survived after acid leaching were uniformly distributed in the S, N-doped hierarchical porous carbon matrix at the sub-nanoscale level in FB-CoFe-700, which are believed to contribute to

highly active  $\text{Co}_x\text{-N/S}$  active sites.<sup>45</sup> On the other hand, the extended porous architecture and large specific surface area with a suitable pore volume were easily accessible for oxygen and ions. Moreover, FB-CoFe-700 certainly displayed superior electrocatalytic activity than FB-Co-700 (Figure S7), which corresponded to the speculation above that the Fe etched away created more defects and vacancies in Co particles, thereby increasing the exposed activity sites. Thus, the highly superior electrocatalytic performance of FB-CoFe-700 should be attributed to the best synergy of the fully exposed and well-distributed active sites (graphitic-N, pyridinic-N,  $\text{CoO}_x$ ,  $\text{Co-N}_x$ , and  $\text{Co-S}_x$ ) and the easily accessible porous structure achieved at  $700^\circ\text{C}$ .

To further explore the kinetics information of the catalysts, FB-CoFe-700 was investigated via RDE voltammetry with various rotation speeds from 400 to 2000 rpm in the  $\text{O}_2$ -saturated 0.1 M KOH electrolyte. As shown in Figure 7c, the diffusion-limiting current density in FB-CoFe-700 electrodes increases with the increasing rotation rate and the diffusion distance becomes shorter at a higher speed. Moreover, the corresponding Koutecky–Levich (K–L) plots based on the LSV curves is obtained to reveal the first-order reaction kinetics for the ORR (Figure 7d). The electron-transfer number was calculated to be 3.97 from the K–L equations, which indicates a dominant four-electron path for FB-CoFe-700-catalyzed ORR in an alkaline medium. The reaction mechanism for FB-CoFe-700 was further studied by the rotating ring-disc electrode (RRDE). The  $n$  value and  $\text{HO}_2^-$  yield were calculated from eqs 4 and 5, respectively. As shown in Figure 7e, within a large potential range of 0.2–0.9 V, the  $\text{HO}_2^-$  yield is less than 8%, and  $n$  is close to 4.0 (Figure 7f). This again confirms a nearly four-electron ORR pathway, which is consistent with the result of RDE.

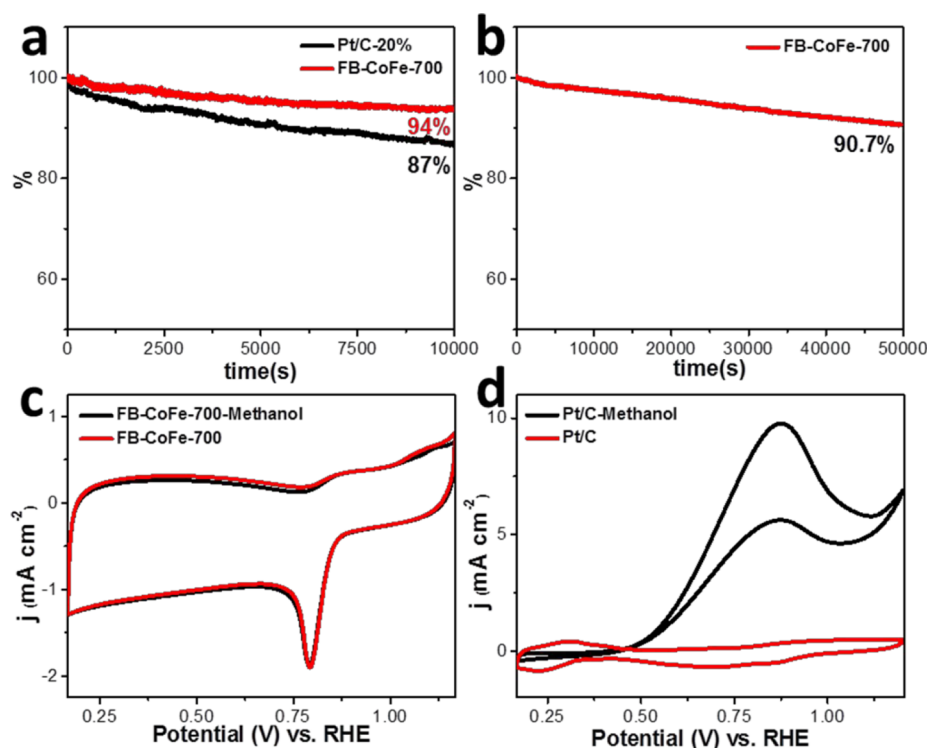


**Figure 8.** Current–time ( $i$ – $t$ ) chronoamperometric response of FB-CoFe-700 and Pt/C 20% for 10 000 s (a) and FB-CoFe-700 for 50 000 s (b) at a rotation speed of 1600 rpm. Methanol crossover effect measurements of (c) FB-CoFe-700 and (d) Pt/C 20% with and without 3 wt % CH<sub>3</sub>OH. All the tests were carried out in O<sub>2</sub>-saturated 0.1 M KOH.

Furthermore, the ORR performance of FB-CoFe-700 in acid media was also tested to show its versatility in electrocatalysis. In Figure S8a, CV measurements conducted in O<sub>2</sub>-saturated 0.5 M H<sub>2</sub>SO<sub>4</sub> reveal the presence of a cathodic peak at 0.55 V (vs RHE) negative than commercial Pt/C (0.74 V vs RHE). The LSV curves in Figure S8b exhibit a little poor onset potential (0.79 V vs RHE), while the  $n$  value calculated based on K–L plots is about 3.9 (Figure S8c). The above results strongly evidence that FB-CoFe-700 displays much better ORR activity in the alkaline medium but potential ORR performance in acidic media.

In addition to the catalytic activity, durability is another key indicator that affects the practical application of ORR catalysts. Therefore, the current–time ( $i$ – $t$ ) chronoamperometric measurements to evaluate the stability of FB-CoFe-700 are performed at 0.7 V (vs RHE) in O<sub>2</sub>-saturated 0.1 M KOH with a scanning speed of 1600 rpm. As displayed in Figure 8a, FB-CoFe-700 exhibits a very slow decay with a high current retention of 94% much superior to commercial Pt/C of only 87% remained after 10 000 s. To further study the stability of FB-CoFe-700, a long-term stability assessment via chronoamperometry up to 50 000 s was performed (Figure 8b). FB-CoFe-700 displays a remarkable ORR electrocatalytic durability, with 90.7% retention of the initial current after 50 000 s. Besides, FB-CoFe-700 under acidic conditions also exhibits a much higher stability of 68% than 43% for commercial Pt/C (Figure S8d). This high stability should be attributed to the well-formed graphitization in the carbon matrix and the steady active sites coexisting with graphitized carbon produced by the CoFe-catalyzed dissolution and reprecipitation process. Moreover, the effect of methanol crossover for FB-CoFe-700 was assessed by CV measurements. As shown in Figure 8c,d, a well-defined cathodic peak can be

clearly observed in O<sub>2</sub>-saturated KOH solution containing methanol without any activity deterioration, indicative of the remarkable methanol tolerance of FB-CoFe-700. In contrast, the Pt/C displays typical methanol oxidation/reduction curves, but the curves are totally absent for oxygen reduction in the same methanol-containing electrolyte, which indicates that FB-CoFe-700 possesses much higher ORR catalytic selectivity than commercial Pt/C. A comparison of ORR activity and stability between FB-CoFe-700 and other reported electrocatalysts is shown in Table S1. Hence, FB-CoFe-700 possesses both much more excellent durability and methanol tolerance than Pt/C, which suggests the potential practical application of FB-CoFe-700 as nonprecious metal ORR electrocatalysts in fuel cells.

#### 4. CONCLUSIONS

In summary, a biomass-derived CoFe/N, S co-doped porous graphitic material (FB-CoFe-700) with multiple CoFe structures including hollow, core–shell, and solid structures was facilely prepared by the thermal pyrolysis of FB and a metal source followed by the acid treatment process. Thanks to the excellent synergy effect of the porous structure with fully exposed and well-distributed active sites (graphitic-N, pyridinic-N, CoO<sub>*x*</sub>, Co–N<sub>*x*</sub>, and Co–S<sub>*x*</sub>) and graphitic carbon-encased metal nanoparticles with the coexistence of graphitized nanoribbons, FB-CoFe-700 exhibited remarkable long-term electrocatalytic stability and outstanding methanol-resistance much superior to commercial Pt/C as well as promising ORR catalytic activity in alkaline media. Moreover, the process of transition metal-catalyzed graphitization was investigated and summarized. This work provided new theoretical support for further advancement on nonprecious metal electrocatalysts with long-term durability.

## ■ ASSOCIATED CONTENT

## ■ Supporting Information

The Supporting Information is available free of charge at <https://pubs.acs.org/doi/10.1021/acsomega.1c01024>.

Elemental mapping images of C, N, S, and Co for FB-CoFe-600, FB-CoFe-700, and FB-CoFe-800 (a–c); elemental mapping images of C, N, S, P, and Co for FB-CoFe-700; comparison of elemental distribution mapping for FB-CoFe-600 (a), FB-CoFe-700 (b), and FB-CoFe-800 (c) before acid etching; TEM of FB-CoFe-700 before (a and b) and after (c and d) acid etching; XRD patterns (a) and Raman spectra (b) of FB-CoFe-600, FB-CoFe-700, and FB-CoFe-800; XPS spectra of FB-CoFe-600 (a), FB-CoFe-700 (b), and FB-CoFe-800 (c); LSV curves of FB-Co-700 and FB-CoFe-700 at a rotation speed of 1600 rpm in O<sub>2</sub>-saturated 0.1 M KOH with a scan rate of 10 mV s<sup>-1</sup>; (a) CV curves of FB-CoFe-700 and Pt/C 20% in O<sub>2</sub>-saturated 0.5 M H<sub>2</sub>SO<sub>4</sub> with a scan rate of 10 mV s<sup>-1</sup>; LSV curves (b) and Koutecky–Levich (K–L) plots (c) of FB-CoFe-700 in O<sub>2</sub>-saturated 0.5 M H<sub>2</sub>SO<sub>4</sub> with a scan rate of 10 mV s<sup>-1</sup>; and (d) current–time (*i*–*t*) chronoamperometric response of FB-CoFe-700 and Pt/C 20% in O<sub>2</sub>-saturated 0.5 M H<sub>2</sub>SO<sub>4</sub> at a rotating rate of 1600 rpm for 10 000 s; Comparison of ORR activity and stability between FB-CoFe-700 and other reported electrocatalysts (Table S1) (PDF)

## ■ AUTHOR INFORMATION

## Corresponding Authors

**Hong Li** – School of Chemistry and Chemical Engineering, Frontiers Science Center for Transformative Molecules, Shanghai Key Lab of Electrical Insulation and Thermal Aging, Center of Hydrogen Science, Shanghai Jiao Tong University, Shanghai 200240, P. R. China; [orcid.org/0000-0002-0983-4410](https://orcid.org/0000-0002-0983-4410); Email: [lh102@sjtu.edu.cn](mailto:lh102@sjtu.edu.cn)

**Yongming Zhang** – School of Chemistry and Chemical Engineering, Frontiers Science Center for Transformative Molecules, Shanghai Key Lab of Electrical Insulation and Thermal Aging, Center of Hydrogen Science, Shanghai Jiao Tong University, Shanghai 200240, P. R. China; State Key Laboratory of Fluorinated Functional Membrane Materials, Shandong Huaxia Shenzhou New Material Co. Ltd., Zibo 256401, P. R. China; Email: [ymzhang@sjtu.edu.cn](mailto:ymzhang@sjtu.edu.cn)

## Authors

**Hongjie Meng** – School of Chemistry and Chemical Engineering, Frontiers Science Center for Transformative Molecules, Shanghai Key Lab of Electrical Insulation and Thermal Aging, Center of Hydrogen Science, Shanghai Jiao Tong University, Shanghai 200240, P. R. China

**Supeng Pei** – School of Chemical and Environmental Engineering, Shanghai Institute of Technology, Shanghai 201418, P. R. China

Complete contact information is available at:

<https://pubs.acs.org/doi/10.1021/acsomega.1c01024>

## Notes

The authors declare no competing financial interest.

## ■ ACKNOWLEDGMENTS

This work was supported by the National Key R&D Program of China (2020YFB1505502) and the Center of Hydrogen Science in Shanghai Jiao Tong University and Shanghai Hysun Tech. Co. Ltd. We thank the Instrumental Analysis Center of Shanghai Jiao Tong University for supporting us with XPS, TEM, and ICP tests.

## ■ REFERENCES

- (1) Wang, Y.-J.; Long, W.; Wang, L.; Yuan, R.; Ignaszak, A.; Fang, B.; Wilkinson, D.P. Unlocking the door to highly active ORR catalysts for PEMFC applications: Polyhedron-engineered Pt-based nanocrystals. *Energy Environ. Sci.* **2018**, *11*, 258–275.
- (2) Sui, S.; Wang, X.; Zhou, X.; Su, Y.; Riffat, S.; Liu, C.-J. A comprehensive review of Pt electrocatalysts for the oxygen reduction reaction: Nanostructure, activity, mechanism and carbon support in PEM fuel cells. *J. Mater. Chem. A* **2017**, *5*, 1808–1825.
- (3) Song, Y.; Zhang, X.; Cui, X.; Shi, J. The ORR kinetics of ZIF-derived Fe-N-C electrocatalysts. *J. Catal.* **2019**, *372*, 174–181.
- (4) Feng, C.; Guo, Y.; Qiao, S.; Xie, Y.; Zhang, L.; Zhang, L.; Wang, W.; Wang, J. 2-Methylimidazole as a nitrogen source assisted synthesis of a nano-rodshaped Fe/FeN@N-C catalyst with plentiful FeN active sites and enhanced ORR activity. *Appl. Surf. Sci.* **2020**, *533*, No. 147481.
- (5) Gong, L.; Li, X.; Zhang, Q.; Huang, B.; Yang, Q.; Yang, G.; Liu, Y. Ultrafast and large-scale synthesis of Co<sub>3</sub>O<sub>4</sub> quantum dots-C<sub>3</sub>N<sub>4</sub>/rGO as an excellent ORR electrocatalyst via a controllable deflagration strategy. *Appl. Surf. Sci.* **2020**, *525*, No. 146624.
- (6) Busch, M.; Halck, N.; Kramm, U.; Siahrostami, S.; Krttil, P.; Rossmeisl, J. Beyond the top of the volcano?—A unified approach to electrocatalytic oxygen reduction and oxygen evolution. *Nano Energy* **2016**, *29*, 126–135.
- (7) Chen, Z.; Higgins, D.; Yu, A.; Zhang, L.; Zhang, J. A review on non-precious metal electrocatalysts for PEM fuel cells. *Energy Environ. Sci.* **2011**, *4*, 3167–3192.
- (8) Zhou, X.; Qiao, J.; Yang, L.; Zhang, J. A review of graphene-based nanostructural materials for both catalyst supports and metal-free catalysts in PEM fuel cell oxygen reduction reactions. *Adv. Energy Mater.* **2014**, *4*, No. 1301523.
- (9) Choi, C.; Baldizzone, C.; Polymeros, G.; Pizzutilo, E.; Kasian, O.; Schuppert, A.; Ranjbar Sahraie, N.; Sougrati, M.-T.; Mayrhofer, K. J. J.; Jaouen, F. Minimizing operando demetallation of Fe-N-C electrocatalysts in acidic medium. *ACS Catal.* **2016**, *6*, 3136–3146.
- (10) Choi, C.; Baldizzone, C.; Grote, J.; Schuppert, A.; Jaouen, F.; Mayrhofer, K. Stability of Fe-N-C Catalysts in acidic medium studied by operando spectroscopy. *Angew. Chem. Int. Ed.* **2015**, *54*, 12753–12757.
- (11) Chenitz, R.; Kramm, U.; Lefèvre, M.; Glibin, V.; Zhang, G.; Sun, S.; Dodelet, J. A specific demetallation of Fe-N<sub>4</sub> catalytic sites in the micropores of NC\_Ar + NH<sub>3</sub> is at the origin of the initial activity loss of the highly active Fe/N/C catalyst used for the reduction of oxygen in PEM fuel cells. *Energy Environ. Sci.* **2018**, *11*, 365–382.
- (12) Yang, L.; Shui, J.; Du, L.; Shao, Y.; Liu, J.; Dai, L.; Hu, Z. Carbon-based metal-free ORR electrocatalysts for fuel cells: Past, present, and future. *Adv. Mater.* **2019**, *31*, No. 1804799.
- (13) Banham, D.; Ye, S.; Pei, K.; Ozaki, J.; Kishimoto, T.; Imashiro, Y. A review of the stability and durability of non-precious metal catalysts for the oxygen reduction reaction in proton exchange membrane fuel cells. *J. Power Sources* **2015**, *285*, 334–348.
- (14) Du, R.; Zhang, N.; Zhu, J.; Wang, Y.; Xu, C.; Hu, Y.; Mao, N.; Xu, H.; Duan, W.; Zhuang, L.; Qu, L.; Hou, Y.; Zhang, J. Nitrogen-doped carbon nanotube aerogels for high-performance ORR catalysts. *Small* **2015**, *11*, 3903–3908.
- (15) Gu, J.; Magagula, S.; Zhao, J.; Chen, Z. Boosting ORR/OER activity of graphdiyne by simple heteroatom doping. *Small Methods* **2019**, *3*, No. 1800550.

- (16) Jin, H.; Guo, C.; Liu, X.; Liu, J.; Vasileff, A.; Jiao, Y.; Zheng, Y.; Qiao, S. Emerging two-dimensional nanomaterials for electrocatalysis. *Chem. Rev.* **2018**, *118*, 6337–6408.
- (17) Chung, H.; Cullen, D.; Higgins, D.; Sneed, B.; Holby, E.; More, K.; Zelenay, P. Direct atomic-level insight into the active sites of a high-performance PGM-free ORR catalyst. *Science* **2017**, *357*, 479–484.
- (18) Martinez, U.; Komini, S.; Holby, E.; Chung, H.; Yin, X.; Zelenay, P. Progress in the development of Fe-based PGM-Free electrocatalysts for the oxygen reduction reaction. *Adv. Mater.* **2019**, *31*, No. 1806545.
- (19) Han, C.; Chen, Z. The mechanism study of oxygen reduction reaction (ORR) on nonequivalent P, N co-doped graphene. *Appl. Surf. Sci.* **2020**, *511*, No. 145382.
- (20) Qi, W.; Huang, W.; Niu, J.; Zhang, B.; Zhang, Z.; Li, W. The role of S in the Co-N-S-C catalysis system towards the ORR for proton exchange membrane fuel cells. *Appl. Surf. Sci.* **2021**, *540*, No. 148325.
- (21) Chao, G.; Zhang, L.; Wang, D.; Chen, S.; Guo, H.; Xu, K.; Fan, W.; Liu, T. Activation of graphitic nitrogen sites for boosting oxygen reduction. *Carbon* **2020**, *159*, 611–616.
- (22) Niu, Y.; Huang, X.; Wu, X.; Zhao, L.; Hu, W.; Ming, C. One-pot synthesis of Co/N-doped mesoporous graphene with embedded Co/CoO<sub>x</sub> nanoparticles for efficient oxygen reduction reaction. *Nanoscale* **2017**, *9*, 10233–10239.
- (23) Zhang, R.; Tahir, M.; Ding, S.; Qadeer, M.; Li, H.; Zeng, Q.-X.; Gao, R.; Wang, L.; Zhang, X.; Pan, L. Promotion of nitrogen reserve and electronic regulation in bamboo-like carbon tubules by cobalt nanoparticles for highly efficient ORR. *ACS Appl. Energy Mater.* **2020**, *3*, 2323–2330.
- (24) Cheng, Q.; Han, S.; Mao, K.; Chen, C.; Yang, L.; Zou, Z.; Gu, M.; Hu, Z.; Yang, H. Co nanoparticle embedded in atomically-dispersed Co-N-C nanofibers for oxygen reduction with high activity and remarkable durability. *Nano Energy* **2018**, *52*, 485–493.
- (25) Meng, H.; Chen, X.; Gong, T.; Liu, H.; Liu, Y.; Li, H.; Zhang, Y. N, P, S/Fe-codoped carbon derived from feculae bombycis as an efficient electrocatalyst for oxygen reduction reaction. *ChemCatChem* **2019**, *11*, 6015–6021.
- (26) Li, L.; Song, L.; Guo, H.; Xia, W.; Jiang, C.; Gao, B.; Wu, C.; Wang, T.; He, J. N-Doped porous carbon nanosheets decorated with graphitized carbon layer encapsulated Co<sub>9</sub>S<sub>8</sub> nanoparticles: An efficient bifunctional electrocatalyst for the OER and ORR. *Nanoscale* **2019**, *11*, 901–907.
- (27) Ya, A.; Marsh, H. Phenomena of catalytic graphitization. Phenomena of catalytic graphitization. *J. Mater. Sci.* **1982**, *17*, 309–322.
- (28) Dhakate, S.; Mathur, R.; Bahl, O. Catalytic effect of iron oxide on carbon/carbon composites during graphitization. *Carbon* **1997**, *35*, 1753–1756.
- (29) Anton, R. In situ TEM investigations of reactions of Ni, Fe and Fe–Ni alloy particles and their oxides with amorphous carbon. *Carbon* **2009**, *47*, 856–865.
- (30) Ohtomo, A.; Hwang, H. A high-mobility electron gas at the LaAlO<sub>3</sub>/SrTiO<sub>3</sub> heterointerface. *Nature* **2004**, *427*, 423–426.
- (31) Anton, R. On the reaction kinetics of Ni with amorphous carbon. *Carbon* **2008**, *46*, 656–662.
- (32) Han, J.; Sa, Y.; Shim, Y.; Choi, M.; Park, N.; Joo, S. H.; Park, S. Coordination chemistry of [Co(acac)<sub>2</sub>] with N-doped graphene: Implications for oxygen reduction reaction reactivity of organometallic Co-O<sub>4</sub>-N Species. *Angew. Chem., Int. Ed.* **2015**, *54*, 12622–12626.
- (33) Wang, H.; Yin, F.; Chen, B.; He, X.; Lv, P.; Ye, C.; Liu, D. ZIF-67 incorporated with carbon derived from pomelo peels: A highly efficient bifunctional catalyst for oxygen reduction/evolution reactions. *Appl. Catal., B* **2017**, *205*, 55–67.
- (34) Zhu, Y.; Liu, Y.; Liu, Y.; Ren, T.; Du, G.; Chen, T.; Yuan, Z. Heteroatom-doped hierarchical porous carbons as high-performance metal-free oxygen reduction electrocatalysts. *J. Mater. Chem. A* **2015**, *3*, 11725–11729.
- (35) Meng, H.; Liu, Y.; Liu, H.; Pei, S.; Yuan, X.; Li, H.; Zhang, Y. ZIF67@MFC-derived Co/N-C@CNFs interconnected frameworks with graphitic carbon-encapsulated Co nanoparticles as highly stable and efficient electrocatalysts for oxygen reduction reactions. *ACS Appl. Mater. Interfaces* **2020**, *12*, 41580–41589.
- (36) Zhang, B.; Lin, Z.; Huang, J.; Cao, L.; Wu, X.; Yu, X.; Zhan, Y.; Xie, F.; Zhang, W.; Chen, J.; Mai, W.; Xie, W.; Meng, H. Highly active and stable non noble metal catalyst for oxygen reduction reaction. *J. Hydrogen Energy* **2017**, *42*, 10423–10434.
- (37) Zhang, C.; Lu, B.; Cao, F.; Wu, Z.; Zhang, W.; Cong, H.; Yu, S. Electrospun metal-organic framework nanoparticle fibers and their derived electrocatalysts for oxygen reduction reaction. *Nano Energy* **2019**, *55*, 226–233.
- (38) Jo, W.; Morub, S.; Leed, D.; Tond, S. Cobalt- and iron-coordinated graphitic carbon nitride on reduced graphene oxide: A nonprecious bimetallic M-N<sub>x</sub>-C analogue electrocatalyst for efficient oxygen reduction reaction in acidic media. *Appl. Surf. Sci.* **2020**, *531*, No. 147367.
- (39) Yan, Y.; Li, K.; Chen, X.; Yang, Y.; Lee, J. Heterojunction-assisted Co<sub>3</sub>S<sub>4</sub>@Co<sub>3</sub>O<sub>4</sub> core-shell octahedrons for supercapacitors and both oxygen and carbon dioxide reduction reactions. *Small* **2017**, *13*, No. 1701724.
- (40) Li, H.; Huang, Y.; Zhou, H.; Yang, W.; Li, M.; Huang, Z.; Fu, C.; Kuang, Y. One step in situ synthesis of Co@N, S co-doped CNTs composite with excellent HER and ORR bi-functional electrocatalytic performances. *Electrochim. Acta.* **2017**, *247*, 736–744.
- (41) Zhang, Y.; Chao, S.; Wang, X.; Han, H.; Bai, Z.; Yang, L. Hierarchical Co<sub>9</sub>S<sub>8</sub> hollow microspheres as multifunctional electrocatalysts for oxygen reduction, oxygen evolution and hydrogen evolution reactions. *Electrochim. Acta* **2017**, *246*, 380–390.
- (42) Qiao, X.; Jin, J.; Fan, H.; Li, Y.; Liao, S. In situ growth of cobalt sulfide hollow nanospheres embedded in nitrogen and sulfur co-doped graphene nanoholes as a highly active electrocatalyst for oxygen reduction and evolution. *J. Mater. Chem. A* **2017**, *5*, 12354–12360.
- (43) Han, H.; Bai, Z.; Wang, X.; Chao, S.; Liu, J.; Kong, Q.; Yang, X.; Yang, L. Highly dispersed Co nanoparticles inlayed in S, N-doped hierarchical carbon nanoprisms derived from Co-MOFs as efficient electrocatalysts for oxygen reduction reaction. *Catal. Today* **2018**, *318*, 126–131.
- (44) Zhu, H.; Zhang, J.; Yan, R.; Du, M.; Wang, Q.; Gao, G.; Wu, J.; Wu, G.; Zhang, M.; Liu, B.; Yao, J.; Zhang, X. When cubic cobalt sulfide meets layered molybdenum disulfide: A core-shell system toward synergetic electrocatalytic water splitting. *Adv. Mater.* **2015**, *27*, 4752–4759.
- (45) Peng, X.; Omasta, T.; Magliocca, E.; Wang, L.; Varcoe, J.; Mustain, W. Nitrogen-doped Carbon-CoO<sub>x</sub> nanohybrids: A precious metal free cathode that exceeds 1.0 W cm<sup>-2</sup> peak power and 100 h life in anion-exchange membrane fuel cells. *Angew. Chem., Int. Ed.* **2019**, *58*, 1046–1051.